Designing new Zintl phases SrBaX (X = Si, Ge, Sn) for thermoelectric applications using *ab initio* techniques

Vivek Gusain, Mohd Zeeshan, and B. K. Mani^{1,*}

Slack's phonon-glass and electron-crystal concept has been the guiding paradigm for designing new thermoelectric materials. Zintl phases, in principle, have been shown as great contenders of the concept and thereby good thermoelectric candidates. With this as motivation, we design new Zintl phases SrBaX (X = Si, Ge, Sn) using state-of-the-art computational methods. Herein, we use first-principles simulations to provide key theoretical insights to thermal and electrical transport properties. Some of the key findings of our work feature remarkably low lattice thermal conductivities ($< 1~{\rm W~m^{-1}~K^{-1}}$), putting proposed materials among the well-known thermoelectric materials such as SnSe and other contemporary Zintl phases. We ascribe such low values to antibonding states induced weak bonding in the lattice and intrinsically weak phonon transport, resulting in low phonon velocities, short lifetimes, and considerable anharmonic scattering phase spaces. Besides, our results on electronic structure and transport properties reveal tremendous performance of SrBaGe ($ZT \sim 2.0$ at 700 K), highlighting the relevance among state-of-the-art materials such as SnSe. Further, the similar performances for both p- and n-type dopings render these materials attractive from device fabrication perspective. We believe that our study would invite experimental investigations for realizing the true thermoelectric potential of SrBaX series.

I. INTRODUCTION

Thermoelectricity is one of the promising technologies which could shape the modern world [1]. It can change the way we use our energy resources and could be revolutionary in future power generation [2]. The working principle of a thermoelectric device hinges on the conversion of environment's waste heat into usable electrical energy [3]. An efficient thermoelectric material can power sensors [4], wearables [5], batteries [6], communication devices [7], and remote stations [8], depending on its power output. The efficiency of a thermoelectric material is commonly expressed in terms of figure of merit, i.e., $ZT = S^2 \sigma T / \kappa$, where S, σ , and κ are Seebeck coefficient, electrical conductivity, and thermal conductivity which includes both electronic (κ_e) and thermal (κ_L) contributions [9–11]. Needless to say, a good thermoelectric material should possess a high S, high σ , and low κ . Unfortunately, these parameters are connected with each other posing a tricky optimization challenge [12–14].

Slack [15], in 1995, proposed that a good thermoelectric material should behave like a crystal which eases the flow of current, and simultaneously it should have glass like properties, imparting low κ_L . Such features demand narrow band gap semiconductors with high mobility of charge carriers and minimum thermal conductivity. The formidable requirements are most closely followed by systems comprising elements with small electronegativity differences and heavier atomic masses like Bi, Te, Sb, Sn, Se, and Ge. Likewise Bi₂Te₃ [16] and SnSe [17] are among the best thermoelectric materials with excellent figure of merit values. The small electronegativity dif-

ference renders narrow band gaps, suitable for mobility of charge carriers. On the other hand, heavier elements vibrate slowly and thereby exhibit low phonon velocities, adequate for low κ_L . Slack's concept, also known as PGEC (phonon-glass and electron-crystal), has been the cornerstone in modern day research in thermoelectrics [18].

Though not always necessary, the PGEC requirements make it customary to look for a ternary material at least. In a ternary material, two atoms should form covalent like framework which could facilitate the movement of charge carriers, whereas third atom should have ionic type linkage with the rest framework, conducive to low κ_L . There might be an another possibility that two atoms collectively donate electrons to third, which in turn form isolated anionic chains. The search for such exquisite features in one material narrows down the target to Zintl phases which have been demonstrated to closely follow the PGEC concept to a certain extent [19–21]. A classical description of Zintl phases can be understood in terms of a hypothetical ABX compound, where B and X form a polyanionic framework using electrons donated by A, i.e., $A^{n+}[BX]^{n-}$. Thuswise, $[BX]^{n-}$ can help in electrons movement through lattice and A^{n+} can scatter heat carrying phonons via different mechanisms such as resonant (localized) phonon scattering by rattling modes [22], mass fluctuation [23], and strain field scatterings [24].

Based on the PGEC guidelines as discussed and available literature, our aim is to design new thermoelectric materials using state-of-the-art computational techniques. First-principles simulations give this liberty to design materials by handpicking the desirable elements, provided the material should withstand the rigorous test of its stability. We scanned the periodic table with a zest for unreported materials which could closely abide

¹Department of Physics, Indian Institute of Technology, Hauz Khas, New Delhi 110016, India (Dated: November 11, 2025)

^{*} bkmani@physics.iitd.ac.in

by the PGEC concept. Such prerequisites narrowed down our search to ternary unsynthesized materials comprising heavier earth-abundant elements, and fulfilling the Zintl phase criteria. After testing various possibilities, we arrived at SrBaSn, which fits well our requirements. It is not reported, comprises heavy elements like Ba and Sn which are likely to lower the acoustic phonon frequencies. The heavy elements like Ba and Sn when combined with Sr can improve phonon scatterings on account of mass contrast. Simultaneously, Sr and Ba can also scatter heat carrying phonons by acting as rattler modes. Further, there seems to be a possibility of narrow or moderate band gap in SrBaSn, owing to electronegativity differences between the constituent elements, i.e., ~ 1 for Sr-Sn, Ba-Sn, and 0.06 for Ba-Sn. In addition, SrBaSn can be classified as 1-1-1 type Zintl phases which have gained attention in recent years. With compounds like SrAgSb [25] ($ZT \sim 0.5 \text{ at } 773 \text{ K}$), BaCuSb [26] ($ZT \sim 0.4$ at 1010 K), and NaCdSb [27] ($ZT \sim 1.3$ at 673 K), the 1-1-1 class of Zintl phases have shown tremendous thermoelectric potential. Besides, some first-principles simulations have also predicted lucrative thermoelectric properties, e.g., KSrBi [28] ($ZT \sim 2.8$ at 800 K), NaSrSb $(ZT \sim 1.9)$, and NaBaSb $(ZT \sim 1.0)$ at 900 K [29]. This further strengthens our motivation and make SrBaSn a rational choice for study.

Here, we use state-of-the-art first-principles simulations integrating density functional theory, harmonic and anharmonic lattice dynamics, and solutions of Boltzmann transport equation to evaluate the structural, vibrational, and transport properties of Zintl phases SrBaX (X = Si, Ge, Sn). As stated earlier, the system of primary interest is SrBaSn, however, SrBaSi and SrBaGe are also included for a comprehensive study. These added systems also allow to see the impact of mass contrast and substitution of heavier atom. Our study not only assess the thermoelectric potential of proposed systems but also provide key theoretical insights which could guide future experiments. Some of the highlights of our study include remarkably low room temperature lattice thermal conductivities (< 1 W m⁻¹ K⁻¹), rivaling some of the best materials like PbTe [30], SnSe [17], and Bi₂Te₃ [31]. We find the origin of such low values in weak bonding in the lattice and intrinsically suppressed phonon transport, leading to low phonon velocities and short lifetimes. Further, based on our electronic structure analysis, we find tremendous thermoelectric performance in SrBaGe, arising from its suitable electronic structure favoring high Seebeck coefficient without greatly comprising the electrical conductivity. While SrBaSn turn out to be most efficient at room temperature, further improvement in figure of merit is much needed.

The remainder of the paper is organized in three sections. Section 2 briefly outlines the computational methods used for the study, Sec. 3 discusses results of structural, vibrational, and transport properties, and finally Sec. 4 summarizes the main findings of the work.

II. COMPUTATIONAL METHODS

We performed first-principles simulations based on density functional theory (DFT) as implemented in Vienna ab initio simulation package (VASP) [32, 33] to study the structural, vibrational, and thermoelectric properties of Zintl phases SrBaX (X = Si, Ge, Sn). The projector-augmented wave method was used to treat core and valence electron interactions, combined with the Perdew-Burke-Ernzerhof (PBE) [34] generalized gradient approximation (GGA) for the exchange-correlation functional. The choice of PBE was based on appropriate balance between computational accuracy and efficiency. The plane-wave kinetic energy cutoff was set at 500 eV, after carefully testing the energy and forces convergence within 10^{-8} eV and 10^{-7} eV/Å, respectively.

The structural optimization by relaxing all degrees of freedom was performed using conjugate gradient algorithm. Brillouin zone integration was carried out using a k grid of $11\times11\times11$ for optimization, while a denser grid of $21\times21\times21$ was used for self-consistent energy calculations, which adequately resolves the electronic states close to Fermi level. In addition, modified Becke-Johnson (mBJ) potential [35] was employed for reliable electronic structure, key for obtaining accurate transport properties. Since the proposed systems comprise heavy elements like Ba and Sn, relativistic effects were also included in the electronic structure calculations. To gain insight into chemical bonding and orbital interactions, we calculated crystal orbital Hamilton population (COHP) using Lobster code [36].

Harmonic and anharmonic force constants were obtained using finite displacement method on $2\times2\times2$ supercell (96 atoms), with a default displacement of atoms by 0.01 Å. The supercell size was chosen to reduce finite size effects and considering computational cost. The resulting phonon dispersions were extracted using Phonopy code [37] by solving the equation

$$\sum_{\beta \tau'} D_{\tau \tau'}^{\alpha \beta}(\mathbf{q}) \gamma_{\mathbf{q}j}^{\beta \tau'} = \omega_{\mathbf{q}j}^2 \gamma_{\mathbf{q}j}^{\alpha \tau}.$$
 (1)

where the indices τ, τ' represent the atoms, α, β are the Cartesian coordinates, \mathbf{q} is a wave vector, j is a band index, $D(\mathbf{q})$ is the dynamical matrix, ω is the corresponding phonon frequency, and γ is the polarization vector. The lattice thermal conductivity was evaluated by solving the phonon Boltzmann transport equation (BTE) within the single-mode relaxation time approximation,

$$\kappa_L = \frac{1}{NV} \sum_{\lambda} C_{\lambda} \mathbf{v}_{\lambda} \otimes \mathbf{v}_{\lambda} \tau_{\lambda} \tag{2}$$

where N and V are the number of unit-cells in the crystal and corresponding volume, respectively. The values were converged in terms of cutoff pair distance (5 Å) and q-point mesh (17×17×17). To further gain insight into anharmonic phonon scatterings, we calculated the scattering phase space using ShengBTE code [38].

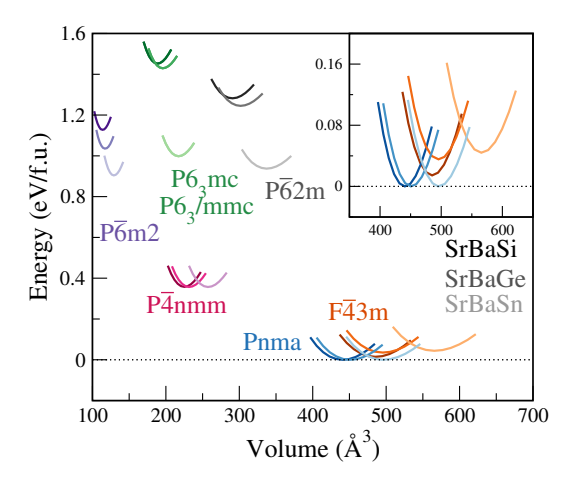


Figure 1. Energy versus volume curves for SrBaSi (dark shade), SrBaGe (medium shade), and SrBaSn (light shade) in different space groups. The inset shows the enlarged view for orthorhombic and cubic space groups. Note that the values overlap for P6₃/mmc and P6₃mc space groups.

The electrical transport properties were calculated by explicitly considering acoustic deformation potential (ADP), ionized impurity (IMP), and polar optical phonon (POP) scattering mechanism as implemented in Amset code [39]. The material related parameters such as elastic constants, dielectric constants, deformation potential, and phonon frequencies were obtained from first-principles simulations to calculate carrier scattering rates. Each scattering mechanism's rate was obtained using Fermi's golden rule [40]

$$\tilde{\tau}_{n\mathbf{k}\to m\mathbf{k}+q}^{-1} = \frac{2\pi}{\hbar} |g_{nm}(\mathbf{k}, \mathbf{q})|^2 \delta(\epsilon_{n\mathbf{k}} - \epsilon_{m\mathbf{k}+q})$$
 (3)

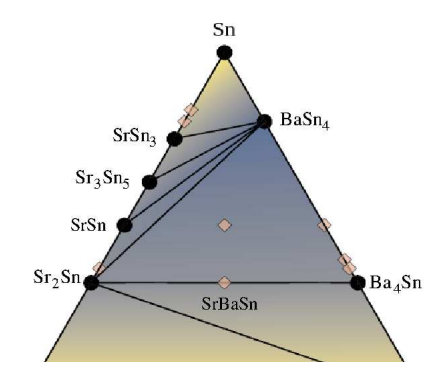
where $n\mathbf{k}$ is the initial wave vector, $m\mathbf{k}+\mathbf{q}$ is the final waver vector, \hbar is the reduced Planck's constant, δ is the Dirac delta function, ϵ is the electron energy, and g is the electron-phonon coupling matrix element. The total carrier scattering rate was obtained by using the Matthiessen's rule [41]

$$\frac{1}{\tau_{\rm e}} = \frac{1}{\tau_{\rm ADP}} + \frac{1}{\tau_{\rm IMP}} + \frac{1}{\tau_{\rm POP}} \tag{4}$$

The coefficients of electrical transport were further tested for convergence in terms of interpolation factor, which was found to be adequate for a default value of 5.

III. RESULTS AND DISCUSSION

In this section, we discuss the crystal structure, its stability, phonon dispersions, electronic structure, and transport properties of SrBaX (X = Si, Ge, Sn) systems.



Fi th re

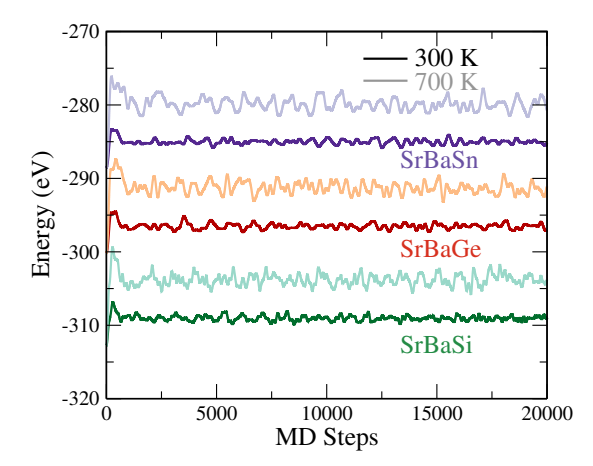


Figure 3. Energy evolution for *ab initio* molecular dynamics simulations as a function of steps for SrBaX (X = Si, Ge, Sn) at 300 and 700 K.

A. Structural Stability

SrBaX (X = Si, Ge, Sn), these materials are not experimentally reported. Therefore, finding the right crystal structure is pivotal. We stress upon the stability of these materials and address the question in a hierarchical fashion. Literature reveals that ternary XYZ type materials containing alkali or alkaline earth metals along with main group element more often crystallize in cubic, hexagonal, tetragonal, and orthorhombic symmetries [42, 43]. The respective prototype structures are MgAgAs-type, [LiGaGe, ZrNiAl, BaLiSi, ZrBeSi-type], PbClF-type, and TiNiSi-type. Likewise, we optimized SrBaX materials in these mentioned space groups. The crystallographic parameters were adopted from their nearest reported material, e.g., using SrMgSn [44] for orthorhombic SrBaSn, among others. The energies of SrBaX systems in the respective symmetries are shown as a function of volume in

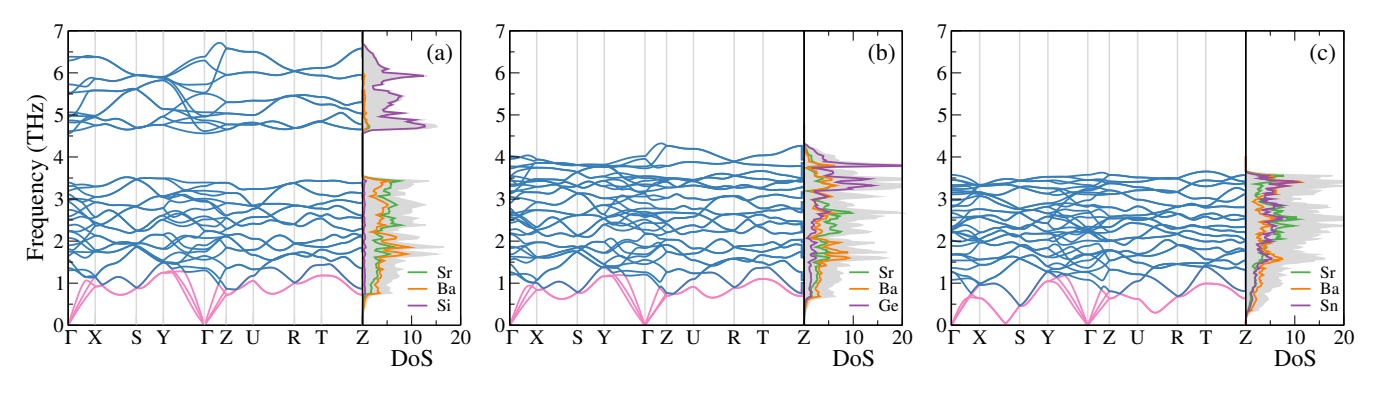


Figure 4. Phonon dispersion curves and density of states (in arb. units) for (a) SrBaSi, (b) SrBaGe, and (c) SrBaSn.

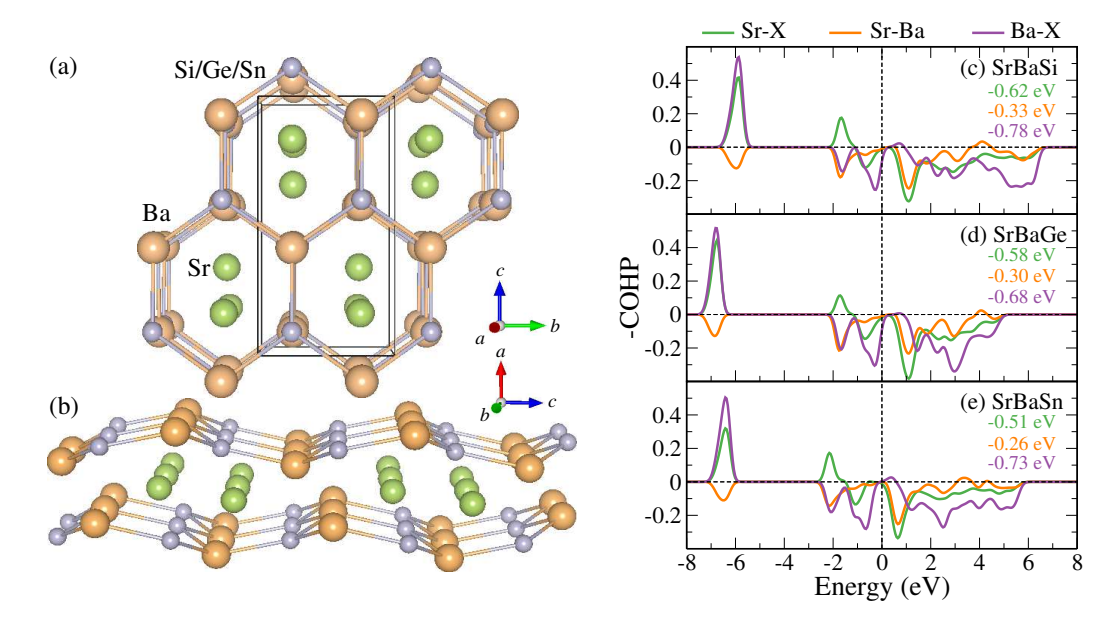


Figure 5. (a) Crystal structure of SrBaX (X = Si, Ge, Sn) in orthorhombic Pnma space group and (b) sideview of the structure showing puckered hexagonal rings of Ba and X atoms along bc-plane, while Sr atoms are stacked along a-axis, (c)-(e) crystal orbital Hamilton population of SrBaSi, SrBaGe, and SrBaSn, respectively. The numerical values represent integrated crystal orbital Hamilton populations for different interaction pairs.

Fig. 1. Interestingly, all three systems have lowest energy in orthorhombic phase. Only the cubic symmetry competes with orthorhombic to some extent, whereas hexagonal and tetragonal structures have markedly higher energies. The shape of the energy well further hints at static stability of the structures.

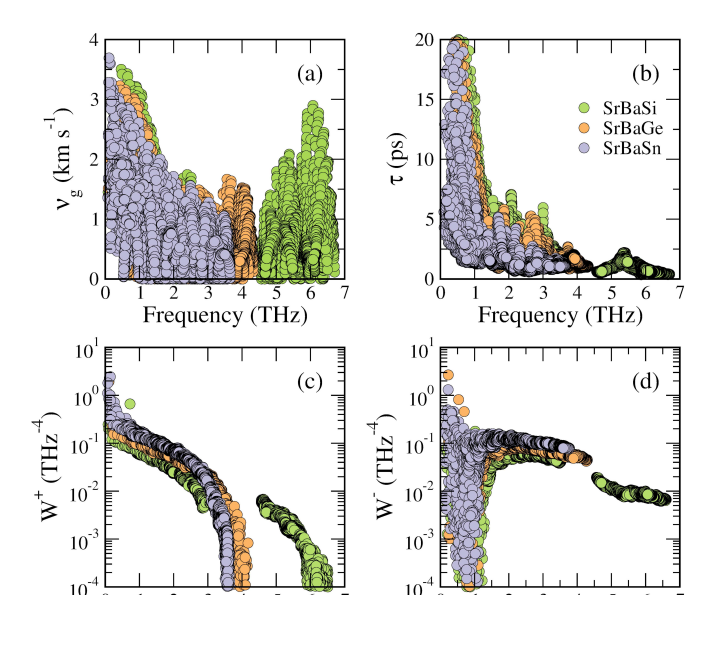
Ascertaining that SrBaX systems can crystallize in orthorhombic symmetry, we delve deeper into their stability. We first assess the thermodynamic favorability in terms of formation energies (ΔE), calculated using the expression

$$\Delta E = E_{SrBaX} - (E_{Sr} + E_{Ba} + E_X) \tag{5}$$

where E_{SrBaX} is the total energy per formula unit, and E_{Sr} , E_{Ba} , and E_{X} are the energies of respective elements per atom. Our calculated formation energy values are negative, i.e., $\Delta E = -0.90$, -1.42, and -1.74 eV/atom for SrBaSi, SrBaGe, and SrBaSn, respectively, indicat-

ing their synthesis is exothermic and materials are stable with respect to their constituent elements. More negative value in the case of SrBaSn hints at enhanced stability under ambient conditions. Though formation energy is a key ingredient of stability, it merely tells that a material is energetically favorable. A material can have negative formation energy and could still decompose into other compositions in the same chemical space.

A true test of thermodynamic stability requires to construct a convex hull from all known phases within the relevant chemical space. We constructed convex hull for Sr-BaX materials using the OQMD database [45, 46], which comprises binary and ternary phases reported experimentally, along with hypothetical possibilities based on common structural prototypes. As discernible from Fig. 2 and Fig. S1-S2, SrBaSn, and SrBaSi/Ge, respectively, lie slightly above the convex hull. The respective energy distance from the hull, ΔE_{HD} , are 0.037, 0.035, and 0.032



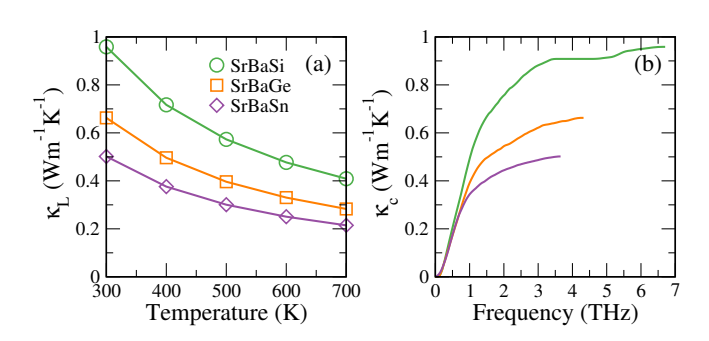


Figure 7. (a) Average lattice thermal conductivity as a function of temperature and (b) cumulative lattice thermal conductivity at 300 K as a function of phonon frequency.

eV/atom. By definition, any phase that sits on the convex hull is thermodynamically stable at 0 K. Having said that, for materials which do not lie on the convex hull, the likelihood of synthesis cannot be completely ruled out. In such cases, the energy distance from the convex hull becomes the defining parameter. For instance, Ma et al. [47] noted that 90 experimentally reported materials lie close to hull distance within 0.1 eV/atom. It can thus be surmised that SrBaX may not be strictly stable at 0 K, however, the small distances from the convex hull do not preclude experimental synthesis or metastability to say the least. We believe that finite temperature synthesis can sustain such metastability and these materials could be experimentally accessible.

To probe the finite temperature stability, we performed *ab initio* molecular dynamics (AIMD) simulations at 300 and 700 K for SrBaX systems over 20,000 MD steps, with

step size of 0.5 fs. As shown in Fig. 3, at 300 K, the energies across the systems fluctuate narrowly without any drastic changes. Even at higher temperature of 700 K, when the thermal vibrations are more pronounced, the oscillations are bounded around the mean position. Such behavior indicates the structural integrity, robustness, and unlikeliness of systems to undergo any collapse or irreversible bond breaking at finite temperature. We further checked the mechanical stability of the compounds by means of elastic constant values. For an orthorhombic phase, a stable crystal structure should follow the Born–Huang elastic stability criteria [48], i.e.,

$$C_{11} > 0, C_{11}C_{12} > C_{12}^2$$
 (6a)

$$C_{11}C_{22}C_{23} + 2C_{12}C_{13}C_{23} - C_{11}C_{23}^2 - C_{22}C_{13}^2 - C_{33}C_{12}^2 > 0$$
(6b)

$$C_{44} > 0, C_{55} > 0, C_{66} > 0$$
 (6c)

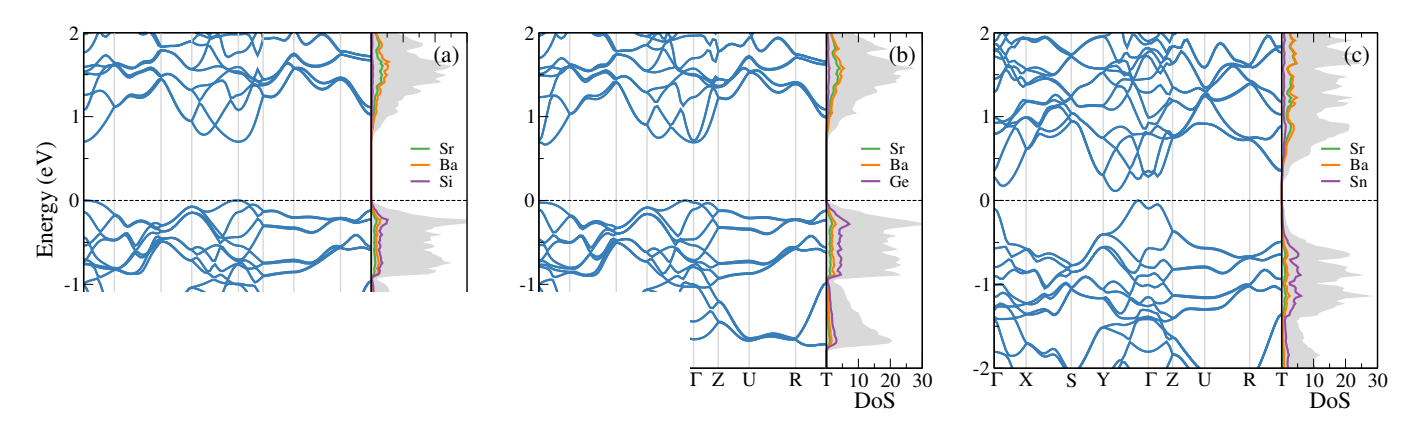
Our calculated elastic constant values, as listed in Supplemental Material [49], obey the stability criteria and highlight the mechanical stability of these systems.

In the hierarchy of stability, we lastly checked the dynamical stability of the systems through phonon dispersions. We observe from Fig. 4 that there are no imaginary frequencies throughout the Brillouin zone for all three systems, indicating their resistance to any structural distortions. To summarize thus far, based on energy profile, formation energy, convex hull analysis, AIMD simulations, and phonon dispersions, we have demonstrated the stability of SrBaX (X = Si, Ge, Sn) systems in orthorhombic phase. Now we proceed to look at the crystal structure arrangement and the bonding features in orthorhombic symmetry.

B. Crystal Structure and Bonding

The crystal structure of SrBaX (X = Si, Ge, Sn) in orthorhombic symmetry emulates the well-known TiNiSi structural prototype in Pnma space group. The TiNiSitype structure has been discussed in lengths in literature [50]. Here, we briefly recapitulate the essential structural aspects central to the theme of our work. The crystal structure has puckered six-membered rings of Ba-X stacked along yz-plane, whereas Sr-atoms are centered along x-axis between two such hexagonal rings, as shown in Fig. 5. The nearest neighbor distance for X-X atoms is of the order of ~ 5 Å, suggesting no bonding interactions among them and ruling out any possibility of anionic framework for $[X-X]^{n-}$. This is an indication of $[Ba-X]^{n-}$ type network, whereas the Sr atoms are weakly linked to the rest framework. To gain a better understanding, we performed the -COHP analysis for predicting bonding features in a crystal lattice.

The -COHP interactions for Sr-Ba, Sr-X, and Ba-X pairs are shown in Fig. 5(c)-(e). In all three systems, bonding interactions are prevalent well below the Fermi level. The dominant interactions are particularly for Ba-X, followed by Sr-X, as can be noticed by large posi-



ates of (a) SrBaSi, (b) SrBaGe, and (c) SrBaSn.

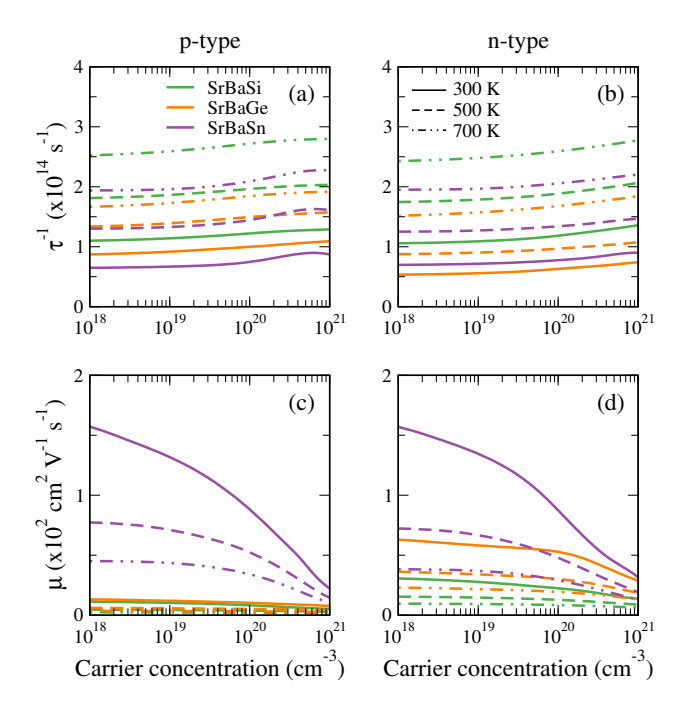


Figure 9. (a), (b) Scattering rates and (c), (d) carrier mobility for p-type and n-type carrier concentration, respectively, at different temperatures for SrBaX (X = Si, Ge, Sn).

tive -COHP peaks in the region of -5 to -8 eV for different systems. The integrated COHP (ICOHP) values provide a quantitative measure of bonding strength and further substantiates the stronger bonding interactions in Ba-X (-0.78 eV, -0.68 eV, and -0.73 eV, respectively). This suggests the $[\text{Ba-X}]^{n-}$ type framework in the lattice, whereas Sr-atoms can act as electropositive entity donating charge to the lattice, consistent with the Zintl concept. Furthermore, the decreasing ICOHP values demonstrate gradual reduction in bonding strength on going from SrBaSi to SrBaSn, highlighting the relative phonon softening and suppressed thermal transport.

Notably, there are prominent antibonding states for Ba-X and Sr-X interactions just below the Fermi level in the valence band maxima, indicating weak bonding

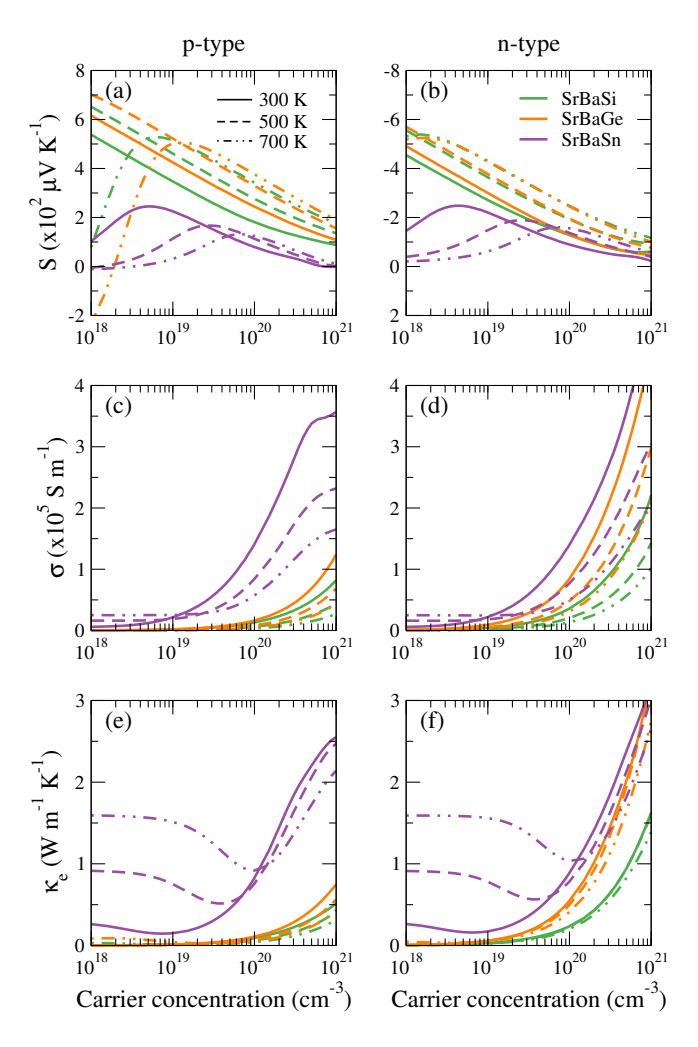


Figure 10. (a), (b) Seebeck coefficient, (c), (d) electrical conductivity, and (e), (f) electronic thermal conductivity, for p-type and n-type carrier concentration, respectively, at different temperatures for SrBaX (X = Si, Ge, Sn).

in the lattice. Such antibonding states result in softer phonon modes [28] and reduced phonon group velocities, as discussed in the following section.

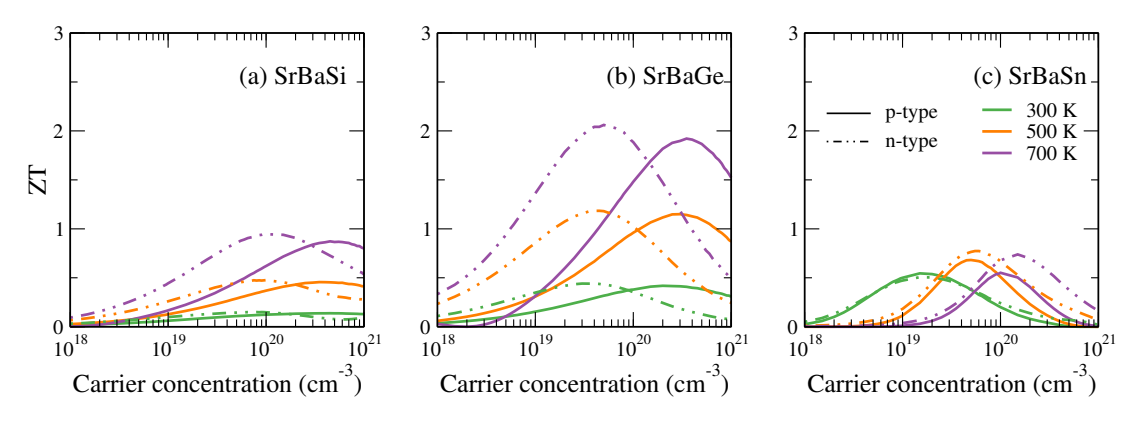


Figure 11. Figure of merit as a function of carrier concentration at different temperatures for p-type and n-type (a) SrBaSi, (b) SrBaGe, and (c) SrBaSn.

C. Phonons and Lattice Thermal Conductivity

In addition to dynamic stability, as noticed from Fig. 4, now we revisit phonon dispersions from the viewpoint of thermal transport. In total, there are 36 phonon modes per wave vector, originating from 12 atoms in the primitive unit cell. Generally, the phonon modes are organized hierarchically in order of atomic masses of constituent elements. In a broader aspect, the lighter atoms (Si, Ge) contribute to the high-frequency optical modes, whereas heavier atoms (Sr, Ba) participate dominantly in the acoustic modes for SrBaSi/Ge. Since the size difference of constituent elements in SrBaSn is not as substantial as rest materials, it displays a mixed behavior. For instance, the Sn atoms have a greater say in high-frequency phonon modes, whereas the acoustic modes are dominated by Ba atoms, with significant contributions of Sr and Sn atoms as well.

There is a noticeable bunching of phonon modes as one go from SrBaSi (6.5 THz) to SrBaGe (4.5 THz), and to SrBaSn (3.5 THz), pointing at smaller slopes of phonon modes. Since the slope of the phonon modes correspond to phonon group velocities, i.e., $\nu_q = d\omega/dq$, all materials are expected to have low phonon velocities, as shown in Fig. 6(a). The respective average sound velocities are significantly low, i.e., 2.34, 2.20, and 2.02 ${\rm km~s^{-1}}$, which puts them in-line with renowned materials such as SnSe [17], PbTe [30], and Bi₂Te₃ [31]. The ν_q shows a decreasing trend with phonon frequencies on going from Si to Sn, depicting the effect of increasing atomic mass and weak bonding in the lattice. In SrBaSi, acoustic modes reaches ~ 3 km s⁻¹, the mid-frequency phonon modes span close to $\sim 1.5 \text{ km s}^{-1}$, and the high frequency modes above the phonon gap also have reasonable contribution, consistent with the dispersive nature of phonons and hints at stronger interactions among atoms. SrBaGe has slightly lower ν_q values and the dispersions are confined to 4.3 THz, reflecting the softening of phonon modes. In SrBaSn, the majority of acoustic modes lie below ~ 2 km s⁻¹, whereas the most optical modes are clustered below 1 km s⁻¹, correlating with the flat phonon modes. The reduced ν_g in SrBaSn is testament to intrinsically weak phonon transport and pronounced acoustic-optical coupling, also indicating short phonon lifetimes.

The frequency dependent phonon lifetimes (τ) of Sr-BaSi, SrBaGe, and SrBaSn are presented in Fig. 6(b). The lifetimes decrease rapidly with frequencies due to enhanced anharmonic phonon-phonon scatterings. The majority of phonon modes in the region below 1.5 THz have lifetimes within 10 ps, reminiscent of distinguished material SnSe [51]. In particular, SrBaSi depicts relatively longer lifetimes across the frequency range, consistent with its more dispersive phonon modes in comparison to rest materials. Notably, SrBaSn exhibits the shortest lifetimes with most modes lying well below 4 ps across the spectrum, in agreement with its relatively flat phonon modes, low group velocities, and strong acousticoptical mixing. The lifetimes of SrBaGe show an intermediate behavior and lie approximately in between those of SrBaSi and SrBaSn. Importantly, such low lifetimes suggest pronounced anharmonicity in the crystal lattice.

To delve deeper into thermal transport, we next study the three-phonon anharmonic scattering phase spaces for SrBaX systems for absorption (W⁺) and emission (W⁻) processes as shown in Fig. 6(c)-(d). For low frequency phonon modes (< 1.5 THz), W⁺ is higher, suggesting dominance of absorption processes for acoustic modes. Across the materials, W⁺ decreases rapidly with frequency, showing the typical inverse relation between scattering and frequency. SrBaSn exhibits the largest W⁺ values for most of the region, substantiating its short phonon lifetimes. On the other hand, SrBaSi shows lowest values, indicating relatively weak phonon-phonon interactions and accordingly higher lifetimes. Yet again, SrBaGe displays intermediate values. The shorter W⁺ for optical modes, especially high frequency ones, corroborates that heat transport is predominantly governed by the acoustic modes. Further, W⁻ gradually increases with frequency and peaks around 1.5 THz, indicating acoustic-optical mixing. Thereafter, W⁻ consistently decreases with increasing frequency. Once again SrBaSn

show larger W⁻, SrBaSi lowest, and SrBaGe lies in between. Overall, the analysis of anharmonic scattering phase spaces points at weaker thermal transport in SrBaSn in comparison to other counterparts.

The collective behavior of phonon group velocities, lifetimes, and scattering phase spaces implies severely hindered thermal transport in SrBaSn in comparison to Sr-BaSi, whereas SrBaGe shows moderate behavior. Likewise, as discernible from Fig. 7, we obtained the trend of average κ_L in the order of SrBaSi > SrBaGe > Sr-BaSn. As a matter of fact, the κ_L values are nearly half for SrBaSn in comparison to SrBaSi. Further, the κ_L decreases with increasing temperature on account of enhanced phonon-phonon scatterings at higher temperatures. It is interesting to note that the κ_L values range 0.95-40, 0.66-0.28, and $0.50-0.21 \text{ W m}^{-1} \text{ K}^{-1}$ in the temperature region of 300-700 K for SrBaSi, SrBaGe, and SrBaSn, respectively. These numbers correlate fairly well with well-known thermoelectric materials like SnSe $\begin{array}{l} (\kappa_L \sim 0.47~{\rm W~m^{-1}~K^{-1}})~[17],~{\rm PbTe}~[30]~(\kappa_L \sim 2.0~{\rm W} \\ {\rm m^{-1}~K^{-1}}),~{\rm and}~{\rm Bi}_2{\rm Te}_3~[31]~(\kappa_L \sim 1.6~{\rm W~m^{-1}~K^{-1}}), \end{array}$ and also with some other 1-1-1 type Zintl phases such as BaCuSb [26] and NaCdSb [27], suggesting the thermoelectric potential of studied systems, especially SrBaSn.

Such phenomenally low values intrigued us to further gain insights into atomic contributions toward κ_L . Hence, we calculated cumulative κ_L as a function of phonon frequency. At 300 K, the low frequency phonon modes up to 2.0 THz contribute extensively to the κ_L , i.e., 88% in SrBaSn to 80% in SrBaSi. In conjunction with Fig. 4, we observe that these modes are predominantly contributed by Sr and Ba atoms in SrBaSi/Ge, whereas Ba has major contribution in the case of SrBaSn. Thus, any attempt to lower the κ_L should target doping at alkaline earth metal (Sr, Ba) sites. The favorable dopants could be lighter atoms like Y and Ce, acting as scattering centers which could disrupt the phonon propagation. For instance, Tihtih et al. [52] demonstrated the reduction of κ_L in Sr and Y-doped BaTiO₃. Further, the Sr-rich or Ba-deficient compositions can also help in lowering the κ_L , as observed in another study. Sr-doped BaTiO₃ showed lattice disorder facilitating the scattering of phonons [53].

Altogether, these materials demonstrate hindered thermal transport and invites further exploration of electrical transport properties from the viewpoint of thermoelectric performance. The electrical transport properties are derived exploiting electronic structure and scattering rates, as discussed in the following section.

D. Electronic structure and Transport Properties

The electronic band structures and density of states of SrBaX are presented in Fig. 8. All the materials are semiconducting in nature, beneficial from the perspective of thermoelectrics. While only the lighter composition SrBaSi displays direct bandgap of 0.69 eV along

Γ-point, SrBaGe shows an indirect bandgap of 0.66 eV, whereas the value is drastically reduced to 0.11 eV in the case of heavier SrBaSn. Such low bandgap may promote bipolar conduction in SrBaSn. Though all the materials show similar overall topology, but there are slight variations in the position and curvature of the bands near the Fermi level, which have direct relevance to the transport properties. All systems have more dispersive bands in the conduction band region in comparison to valence band region. Thus, p-type systems are likely to exhibit higher Seebeck coefficients, whereas higher electrical conductivities for n-type systems. SrBaSi and SrBaGe have relatively more flat bands in the valence band region in comparison to SrBaSn, indicating larger Seebeck coefficients for p-type systems. Meanwhile, the conduction band minima of SrBaSn has relatively more dispersive nature of bands in comparison to others. Thus, in conjunction with reduced bandgap, SrBaSn is likely to exhibit enhanced electrical conductivities in comparison to other counterparts.

It is interesting to note that in addition to valence band maximum (VBM), there is a second valley along Γ -Z direction within 0.05 eV energy window in all the cases. Such multiple valleys facilitate the mobility of charge carriers and improve power factor [54]. To shed more light on the electronic states near the Fermi level, we further analyzed the projected density of states (DoS). The states close to Fermi level in the valence band maxima are majorly contributed by X atoms (X = Si, Ge, Sn), consistent with their greater electronegativity, whereas Sr and Ba atoms dominate in the conduction band minima. The DoS features further compliment the analysis of electronic bands. SrBaSi and SrBaGe exhibit sharper, more localized DoS at the valence band edges, whereas SrBaSn displays a broader distribution. These observations in SrBaSi and SrBaGe suggest larger effective mass and more localization of carriers close to valence band extrema, while SrBaSn promotes lighter carriers with enhanced velocities.

Based on the electronic structure, our calculated net scattering rates and mobility of charge carriers are shown in Fig. 9. The various components of scattering rates, viz., ADP, IMP, and POP, as shown in Fig. S8, demonstrate the dominance of POP scattering for SrBaSi and SrBaGe at considered temperatures (300, 500, and 700 K). While SrBaSn show similar behavior at moderate temperatures, ADP is the dominating mechanism at 700 K. This shows that, except for the latter case, charge carriers interact more with polar optical phonons. Nonetheless, the net scattering rates increase steadily with carrier concentrations and rapidly with temperature for both p- and n-type dopings. Overall, the net scattering rates range 0.8-2.7 fs⁻¹ and 0.7-2.7 fs⁻¹ for holes and electrons, respectively.

Now, we move to the other aspect of Fig. 9, i.e., mobility of charge carriers, which play an important role in understanding the transport behavior. Mobility of carriers is a cumulative effect of scattering rates, band disper-

sions, and effective mass of charge carriers. For SrBaSi and SrBaGe, electrons show higher mobilities in comparison to holes, on account of more dispersive bands in conduction band minima. On the other hand, SrBaSn has similar mobilities for both holes and electrons, consistent with dispersive bands near either band edges. The notable observation is the standout anomalously high mobility of SrBaSn, originating collectively from its small bandgap (0.11 eV) and highly dispersive bands close to band extrema. Further, the decreasing mobility trend with carrier concentration and temperature is consistent with frequent scatterings and increased thermal motion of charge carriers. Following this analysis, we next evaluate the resulting electrical transport properties.

As discernible from Fig. 10, from a broader perspective, SrBaGe exhibits largest Seebeck coefficients at 300 and 500 K, SrBaSi show larger values at 700 K for small carrier concentrations, whereas SrBaSn has lowest numbers. This can be attributed to flat bands and larger density of states close to band edges in SrBaSi and SrBaGe with respect to SrBaSn, as illustrated in Fig. 8. At 300 and 500 K, Seebeck coefficient for both p- and n-type Sr-BaSi and SrBaGe decreases monotonically with increasing carrier concentrations as the Fermi level moves deeper into the bands. The trend is also consistent with Mott equation for doped semiconductors [55, 56]. However, at 700 K, a pronounced maximum at low to moderate carrier concentrations is observed for holes, whereas a tiny glimpse of the same can be seen for electrons. Such behavior at high temperatures is often associated with bipolar conduction, especially in materials with narrow band gap, for instance, SrBaSn ($E_q \sim 0.11 \text{ eV}$) in the present study. Unlike SrBaSi and SrBaGe, SrBaSn demonstrate bipolar effects throughout the considered temperatures, for both holes and electrons.

In contrast, electrical conductivity benefits from such phenomenon because both electrons and holes can jointly contribute, as can be noticed from Fig 10. SrBaSn has phenomenally higher σ in comparison to SrBaSi and SrBaGe. The trend is in agreement with the dispersive bands and significantly higher mobilities of charge carriers. In general, the electrons have higher conductivities in SrBaSi and SrBaGe, whereas SrBaSn exhibit comparative values for either type of charge carriers. The behavior correlates with the mobilities of charge carriers, as discussed in the context of Fig. 9. Overall, the σ increases with carrier concentration on account of enhanced carriers, and values decrease consistently with temperature due to increased collisions.

However, it should be acknowledged that the downside of bipolar conduction is often elevated electronic thermal conductivities which may harm the overall performance of the material, as observed in the present case. The κ_e of SrBaSi and SrBaGe closely follows the trend of σ . However, κ_e in SrBaSn shows a non-monotonic dependence on carrier concentration on account of bipolar effect. The values are nearly constant at the low doping level, then decreasing over an intermediate dopings, and finally in-

creasing at higher dopings. Notably, SrBaSn has significantly higher κ_e in comparison to other counterparts, which may compensate its phenomenally high σ values. The evolution of S, σ , and κ_e , with temperature and carrier concentration governs the overall thermoelectric performance, as discussed next.

E. Thermoelectric Performance

Figure 11 shows the figure of merit values with respect to carrier concentrations at different temperatures for Sr-BaSi, SrBaGe, and SrBaSn. The conflicting trends of S, σ , and κ_e render a peak in ZT values. In general, ZT increases with temperature in SrBaSi and SrBaGe, whereas the values decrease in SrBaSn beyond 500 K. SrBaGe emerges as standout material exhibiting the highest thermoelectric performance at moderate and high temperature. It attains $ZT \sim 1.1$ at 500 K, and $ZT \sim 1.9$ and 2.0 at 700 K, for p- and n-type dopings, respectively, surpassing both SrBaSi and SrBaSn. It is interesting to note that our calculated values of SrBaGe are competitive with other state-of-the-art materials such as SnSe ($ZT \sim$ 2.6 at 913 K), PbTe-SrTe ($ZT \sim 2.5$ at 923 K), CoSb₃ $(ZT \sim 1.7 \text{ at } 823 \text{ K})$, and other Zintl phases of the same family, e.g., NaCdSb ($ZT \sim 1.3$ at 673 K), and BaCuSb $(ZT \sim 0.4 \text{ at } 1010 \text{ K})$. Nevertheless, the superior performance of SrBaGe can be attributed to delicately balanced electronic structure, resulting in large S without severely comprising σ . In contrast, SrBaSi shows moderate enhancement in ZT with temperature and reaches values close to unity at 700 K. On the other hand, SrBaSn show less improvement in ZT on going from 300 to 500 K, and further undergo decline in ZT at 700 K. The collapse in ZT at high temperature can be attributed to its small band gap, leading to substantial bipolar effects. Thus, despite having large σ values, SrBaSn suffers the simultaneous rise of κ_e . However, SrBaSn show highest values at 300 K among other materials, i.e., $ZT \sim 0.5$.

SrBaSn could be a good thermoelectric prospect at room temperature (300 K), provided its figure of merit could be improved to some extent. We believe that alloying SrBaSn with SrBaGe could help in reducing the bipolar conductivity through bandgap engineering. A modest improvement in bandgap may suppress the larger values of κ_e . Similarly, the performance of SrBaSi can be improved through alloying with SrBaGe, introducing strain in the system [57], or applying hydrostatic pressure [58]. Such techniques can lead to band degeneracy, which has been fruitful in improving power factor. In addition, Sr-BaSi has scope for reducing κ_L through nanostructuring. Besides, an interesting observation is the relatable ZT values for both p- and n-type systems, suitable from the viewpoint of device fabrication. In a thermoelectric module, it is desirable to have both legs of similar material, or ideally of the same material, which is rare. This shows the importance of the SrBaX series in the context of practical applications.

The optimal carrier concentrations for desirable figure of merit values for SrBaGe are of the order of 10^{19} - 10^{20} carriers cm^{-3} for *n*-type dopings, whereas slightly higher carrier concentrations are required for p-type dopings. However, Zintl phases have an intrinsic disposition towards p-type dopings [59, 60]. It is worth mentioning that Toberer et al. [61] reported p-type LiZnSb with carrier concentrations of the order of 10^{20} carriers cm⁻³. The real challenge could be achieving n-type carriers. however, extrinsic dopings could be the pragmatic way ahead. The plausible ways could be introducing aliovalent substitution at cation or X-site. Realistic approach may include substitution on the Sr/Ba-site with trivalent donors such as La³⁺, Ce³⁺, and Y³⁺, or substitution on the group-14 X-site by group-15 dopants (e.g., Sb/Bi on Ge). Similar approaches can be exercised for SrBaSi and SrBaSn. We hope that despite the theoretical nature of present study, our proposed results and recommended guidance would invite further experimental investigations in order to explore the thermoelectric potential of the Sr-BaX series.

IV. CONCLUSION

In this paper, with an aim to design new thermoelectric materials, we have investigated the structural, vibrational, and transport properties of SrBaX (X = Si, Ge, Sn) using state-of-the-art computational methods which combining density functional theory, harmonic and anharmonic lattice dynamics, and solutions of Boltzmann transport equation. Since the chosen materials are not experimentally reported, we rigorously tested their stability through the energy profile, formation energy, convex hull analysis, $ab\ initio$ molecular dynamics simula-

tions, and phonon dispersions. All materials were stabilized in orthorhombic symmetry and show semiconducting behavior (E_q ~ 0.11 -0.69 eV). The -COHP analysis revealed weak bonding in the lattice, conducive to softer phonon modes and reduced phonon group velocities. Our analysis of phonons resulted in weak phonon transport, leading to low phonon velocities, short lifetimes, and enhanced scattering phase space, which are detrimental to thermal conductivity. Likewise, we obtained remarkably low lattice thermal conductivities ($<1 \text{ W m}^{-1} \text{ K}^{-1}$), correlating with well-known thermoelectric materials like SnSe. Based on such low values and combining with electrical transport properties, we obtained tremendous thermoelectric potential in SrBaGe ($ZT \sim 2.0$ at 700 K). While SrBaSn demonstrated anomalously high electrical conductivities, the bipolar conduction severely affected its overall performance. SrBaSi showed ZT values close to unity at 700 K. Nonetheless, the favorable ZT values on either type of dopings, make these materials suitable for device fabrication. We believe that further experimental investigations based on our study would unearth new potential thermoelectric prospects and could serve as motivation for more such studies.

ACKNOWLEDGMENTS

V.G. and M.Z. are thankful to BUKRP00034052 and SERB-DST (File No. PDF/2022/002559), respectively, for the financial assistance. B.K.M. acknowledges the funding support from the SERB, DST (CRG/2022/000178). The calculations were performed using the PARAM Rudra, a national supercomputing facility at the Inter-University Accelerator Centre (IUAC) New Delhi.

- R. Singh, S. Dogra, S. Dixit, N. I. Vatin, R. Bhardwaj, A. K. Sundramoorthy, H. Perera, S. P. Patole, R. K. Mishra, and S. Arya, Hybr. Adv. 5, 100176 (2024).
- [2] F. Garmroudi, A. Riss, M. Parzer, N. Reumann, H. Müller, E. Bauer, S. Khmelevskyi, R. Podloucky, T. Mori, K. Tobita, Y. Katsura, and K. Kimura, Phys. Rev. B 103, 085202 (2021).
- [3] Z. Wehbi, R. Taher, J. Faraj, C. Castelain, and M. Khaled, Energy Rep. 8, 1361 (2022).
- [4] H. Xie, Y. Zhang, and P. Gao, Micromachines 14, 31 (2023).
- [5] Y. Jia, Q. Jiang, H. Sun, P. Liu, D. Hu, Y. Pei, W. Liu, X. Crispin, S. Fabiano, Y. Ma, and Y. Cao, Adv. Mater. 33, 2102990 (2021).
- [6] C. Wang, Y. Niu, J. Jiang, Y. Chen, H. Tian, R. Zhang, T. Zhou, J. Xia, Y. Pan, and S. Wang, Nano Energy 45, 432 (2018).
- [7] M. A. Zoui, S. Bentouba, J. G. Stocholm, and M. Bourouis, Energies 13, 3606 (2020).
- [8] A. Belsky and D. Glukhanich, Renew. Energy Focus 47, 100493 (2023).

- [9] S. Karmakar and T. Saha-Dasgupta, Phys. Rev. Materials 4, 124007 (2020).
- [10] J. Maassen, Phys. Rev. B **104**, 184301 (2021).
- [11] T. Berry, C. Fu, G. Auffermann, G. H. Fecher, W. Schnelle, F. Serrano-Sanchez, Y. Yue, H. Liang, and C. Felser, Chem. Mater. 29, 7042 (2017).
- [12] S. R. Boona, Nature **549**, 169 (2017).
- [13] Y. K. Lee, K. Ahn, J. Cha, C. Zhou, H. S. Kim, G. Choi, S. I. Chae, J.-H. Park, S.-P. Cho, S. H. Park, Y.-E. Sung, W. B. Lee, T. Hyeon, and I. Chung, J. Am. Chem. Soc. 139, 10887 (2017).
- [14] L. E. Bell, Science **321**, 1457 (2008).
- [15] G. A. Slack, in CRC Handbook of Thermoelectrics, edited by D. M. Rowe (CRC Press, Boca Raton, FL, 1995) pp. 407–440.
- [16] F. Serrano-Sánchez, M. Gharsallah, N. M. Nemes, N. Biskup, M. Varela, J. L. Martínez, M. T. Fernández-Díaz, and J. A. Alonso, Sci. Rep. 7, 6277 (2017).
- [17] L.-D. Zhao, S.-H. Lo, Y. Zhang, H. Sun, G. Tan, C. Uher, C. Wolverton, V. P. Dravid, and M. G. Kanatzidis, Nature 508, 373 (2014).

- [18] D. Narducci, "G.S. Nolas al., et semicon-Promising ducting Ge clathrates: candiapplication," dates for thermoelectric in edited by L. Anatychuk, A. Burkov, J. Goldsmid, Y. Grin, K. Koumoto, D. Narducci, and G. S. Nolas (Springer International Publishing, Cham, 2024) pp. 95 - 98.
- [19] J. Wang, M. Guo, J. Zhu, D. Qin, F. Guo, Q. Zhang, W. Cai, and J. Sui, J. Mater. Sci. Technol. 59, 189 (2020).
- [20] A. Balvanz, J. Qu, S. Baranets, E. Ertekin, P. Gorai, and S. Bobev, Chem. Mater. 32, 10697 (2020).
- [21] C. Chen, W. Xue, S. Li, Z. Zhang, X. Li, X. Wang, Y. Liu, J. Sui, X. Liu, F. Cao, Z. Ren, C.-W. Chu, Y. Wang, and Q. Zhang, Proc. Natl. Acad. Sci. U.S.A. 116, 2831 (2019).
- [22] H. Lin, G. Tan, J.-N. Shen, S. Hao, L.-M. Wu, N. Calta, C. Malliakas, S. Wang, C. Uher, C. Wolverton, and M. G. Kanatzidis, Angew. Chem. Int. Ed. 55, 11431 (2016).
- [23] B. Abeles, Phys. Rev. **131**, 1906 (1963).
- [24] J. Yang, G. P. Meisner, and L. Chen Appl. Phys. Lett. 85, 1140 (2004).
- [25] Z. Zhang, Y. Yan, X. Li, X. Wang, J. Li, C. Chen, F. Cao, J. Sui, X. Lin, X. Liu, G. Xie, and Q. Zhang, Adv. Energy Mater. 10, 2001229 (2020).
- [26] S. Zheng, K. Peng, S. Xiao, Z. Zhou, X. Lu, G. Han, B. Zhang, G. Wang, and X. Zhou, J. Adv. Ceram. 11, 1604 (2022).
- [27] K. Guo, Y. Zhang, S. Yuan, Q. Tang, C. Lin, P. Luo, J. Yang, S. Pan, L.-D. Zhao, G. Cheng, J. Zhang, and J. Luo, Angew. Chem. Int. Ed. 62, e202212515 (2023).
- [28] C. Wei, Z. Feng, Y. Yan, G. Zhao, Y. Fu, and D. J. Singh, Phys. Rev. B 108, 235203 (2023).
- [29] C. K. Vishwakarma, M. Zeeshan, and B. K. Mani, J. Phys. Chem. C 128, 2311 (2024).
- [30] D. Bessas, I. Sergueev, H.-C. Wille, J. Perßon, D. Ebling, and R. P. Hermann, Phys. Rev. B 86, 224301 (2012).
- [31] H. Wang, Y. Pei, A. D. LaLonde, and G. J. Snyder, Adv. Mater. 23, 1366 (2011).
- [32] G. Kresse and J. Furthmüller, Comput. Mater. Sci. 6, 15 (1996).
- [33] G. Kresse and J. Furthmüller, Phys. Rev. B 54, 11169 (1996).
- [34] J. P. Perdew, K. Burke, and M. Ernzerhof, Phys. Rev. Lett. 77, 3865 (1996).
- [35] F. Tran and P. Blaha, Phys. Rev. Lett. 102, 226401 (2009).
- [36] S. Maintz, V. L. Deringer, A. L. Tchougréeff, and R. Dronskowski, J. Comput. Chem. 37, 1030 (2016).
- [37] A. Togo and I. Tanaka, Scr. Mater. 108, 1 (2015).

- [38] W. Li, J. Carrete, N. A. Katcho, and N. Mingo, Comp. Phys. Commun. 185, 1747–1758 (2014).
- dates for thermoelectric application," in [39] A. M. Ganose, J. Park, A. Faghaninia, R. Woods-200 Years of Thermoelectricity: An Historical Journey Through the Serience and Technology specific moelectric Materials, (1821-2021), edited by L. Anatychuk, A. Burkov, J. Goldsmid, Nature Commun. 12, 2222 (2021).
 - [40] P. A. M. Dirac and N. H. D. Bohr, Proc. R. Soc. A 114, 243 (1927).
 - [41] A. Matthiessen and C. Vogt, Ann. Phys. 198, 19 (1864).
 - [42] Y. Wang and S. Bobev, Materials 16, 1428 (2023).
 - [43] X. Zhang, L. Yu, A. Zakutayev, and A. Zunger, Adv. Funct. Mater. 22, 1425 (2012).
 - [44] F. Merlo, M. Pani, and M. Fornasini, J. Less-Common Met. 166, 319 (1990).
 - [45] J. E. Saal, S. Kirklin, M. Aykol, B. Meredig, and C. Wolverton, JOM 65, 1501 (2013).
 - [46] S. Kirklin, J. E. Saal, B. Meredig, A. Thompson, J. W. Doak, M. Aykol, S. Rühl, and C. Wolverton, npj Comput. Mater. 1, 15010 (2015).
 - [47] J. Ma, V. I. Hegde, K. Munira, Y. Xie, S. Keshavarz, D. T. Mildebrath, C. Wolverton, A. W. Ghosh, and W. H. Butler, Phys. Rev. B 95, 024411 (2017).
 - [48] F. Mouhat and F. m. c.-X. Coudert, Phys. Rev. B 90, 224104 (2014).
 - [49] See Supplemental Material at [URL] for directional dependent properties, and input parameters.
 - [50] G. A. Landrum, R. Hoffmann, J. Evers, and H. Boysen, Inorg. Chem. 37, 5754 (1998).
 - [51] R. Guo, X. Wang, Y. Kuang, and B. Huang, Phys. Rev. B 92, 115202 (2015).
 - [52] M. Tihtih, J. E. F. Ibrahim, M. A. Basyooni, E. Kurovics, W. Belaid, I. Hussainova, and I. Kocserha, Ceram. Int. 49, 1947 (2023).
 - [53] M. Khalil, M. T. Qureshi, M. A. Elaimi, L. Aamir, M. Ahmad, M. Saleem, and M. Saleem, Results Phys. 67, 108041 (2024).
 - [54] Y. Tang, Z. M. Gibbs, L. A. Agapito, G. Li, H.-S. Kim, M. B. Nardelli, S. Curtarolo, and G. J. Snyder, Nat. Mater. 14, 1223 (2015).
 - [55] J. P. Heremans, V. Jovovic, E. S. Toberer, A. Saramat, K. Kurosaki, A. Charoenphakdee, S. Yamanaka, and G. J. Snyder, Science 321, 554 (2008).
 - [56] M. Cutler and N. F. Mott, Phys. Rev. 181, 1336 (1969).
 - [57] S.-D. Guo and J. Dong, Semicond. Sci. Technol. 33, 085003 (2018).
 - [58] Y. Javed, M. A. Rafiq, and N. Ahmed, RSC Adv. 7, 38834 (2017).
 - [59] S. R. Brown, S. M. Kauzlarich, F. Gascoin, and G. J. Snyder, Chem. Mater. 18, 1873 (2006).
 - [60] X.-J. Wang, M.-B. Tang, J.-T. Zhao, H.-H. Chen, and X.-X. Yang, App. Phys. Lett. 90, 232107 (2007).
 - [61] E. S. Toberer, A. F. May, C. J. Scanlon, and G. J. Snyder, J. App. Phys. 105, 063701 (2009).